Water film-mediated photocatalytic oxidation of oxalate on TiO2

N Tan Luong, Khalil Hanna, Jean-François Boily

Journal of Catalysis 432 (2024) 115425

Contents lists available at ScienceDirect

Journal of Catalysis

journal homepage: www.elsevier.com/locate/jcat

Water film-mediated photocatalytic oxidation of oxalate on TiO_2

N. Tan Luong [a,1,*], Khalil Hanna [b], Jean-François Boily [a]

[a] Department of Chemistry, Umeå University, SE 901 87 Umeå, Sweden
[b] Université de Rennes, École Nationale Supérieure de Chimie de Rennes, CNRS, ISCR-UMR 6226, F-35000 Rennes, France

ARTICLE INFO

Keywords:
Photocatalysis
TiO_2
Water films
Oxalate
Reactive oxygen species
Hydroxyl radicals

ABSTRACT

Water films on minerals under humid environment can be photocatalytic hotspots when exposed to sunlight or artificial sources of ultraviolet (and visible) radiation. In this study, we resolved the water film-mediated photocatalysis of oxalate adsorbed on TiO_2 using *in situ* infrared spectroscopy. We found that 0.5 to 4 monolayer-(ML) thick water films enhanced the photodecomposition rates of oxalate under 21 kPa O_2. We explained this through the combined actions of direct hole transfer, ligand-to-metal-charge transfer, as well as the production of hydroxyl radicals and reactive oxygen species. Rates were, however, substantially slower in the absence of O_2 because charge recombination, together with water film-mediated charge localization, disrupted hole transfer and hydroxyl radical production. Our work adds insight into the impact of humidity on controlling important photocatalytic processes in nature (drying soils, atmospheric aerosols), and technology (water and air treatment).

1. Introduction

Air moisture captured by mineral particles can produce nanometrically-thick water films [1–3] that mediate compositional and structural transformation reactions.[4–8] They can also be photocatalytic hotspots when exposed to sunlight or artificial sources of ultraviolet radiation. For instance, water films formed on atmospheric mineral dust can experience periodic day-night cycles that are responsible for controlling the budget of important pollutants (*e.g.* O_3, SO_x, NO_x, organics) in the troposphere and terrestrial soils through photocatalytic reactions.[8] Understanding of mineral photo-reactivity in the presence of these films is important for fields including atmospheric chemistry, [5,8] geochemistry, [9] water and air purification technology, [10–13] CO_2 utilization, [14] energy production, [15,16] and even space exploration [17].

TiO_2 is an ideal semiconducting model mineral that is beneficial for advancing knowledge on water film-driven photocatalytic reactions. It has a reputably high photocatalytic efficiency on a wide range of substances, [8] is chemically stable, and is appreciably abundant in Earth's continental crust (0.7 % wt.) [18] and atmosphere (0.4–5 %).[8] Anatase and rutile are the most studied and applied TiO_2 phases in photocatalysis, each with different bulk and surface properties (*i.e.*, crystal structure, band structure, defect sites, surface charges, surface OH population, *etc.*) that control charge carrier generation and recombination, and consequently photocatalytic activity.[19,20] TiO_2-driven photocatalytic transformation studies range from fundamental aspects [8,9,19,21–25] to applications [8,9,16,24–27]. While there is an increasing body of work on TiO_2-based catalyst performance (*e.g.*, expanding its working range to visible light), [16,28] novel insights on photocatalytic mechanisms are still urgently needed to broaden working conditions, such as environments that experience large variations in atmospheric humidity [8].

Photocatalytic reactions on TiO_2 generally begin with the photogeneration of electron-hole (e^-/h^+) pairs by light (Fig. 1 a). Unless they recombine, these charge carriers generate (i) hydroxyl radicals ($^\bullet$OH) via direct hole oxidation of surface hydroxo groups ($\equiv OH + h^+ \rightarrow \equiv\square + {}^\bullet OH$) or water ($H_2O + h^+ \rightarrow {}^\bullet OH + H^+$), or (ii) reactive oxygen species (ROS) beginning with the one-electron reduction of oxygen ($O_2 + e^- \rightarrow O_2^{\bullet-}$) (Fig. 1 b). These radicals can then degrade mineral-bound organic molecules, ultimately down to CO_2 and H_2O. Earlier studies revealed that the photo-reactivity of TiO_2 towards organics (*e.g.* phenol, [29] toluene, [30,31] acetic acid, [32] acetaldehyde [32,33] and ethanol [34]) was influenced by water films formed by the condensation of air moisture. Moreover, water films thickness can alter reaction mechanisms and rates [30,33,35,36] by controlling concentrations and distributions of charge carriers and radicals, [33,37–39]. Film thickness can also affect chemical speciation and adsorption modes on TiO_2, including metal-bonded (MB), hydrogen-bonded (HB), or outer-sphere

* Corresponding author.
E-mail address: tan.luong@chalmers.se (N.T. Luong).
[1] Current address: Department of Physics, Chalmers University of Technology, SE 412 96 Gothenburg, Sweden.

https://doi.org/10.1016/j.jcat.2024.115425
Received 22 September 2023; Received in revised form 12 February 2024; Accepted 7 March 2024
Available online 11 March 2024

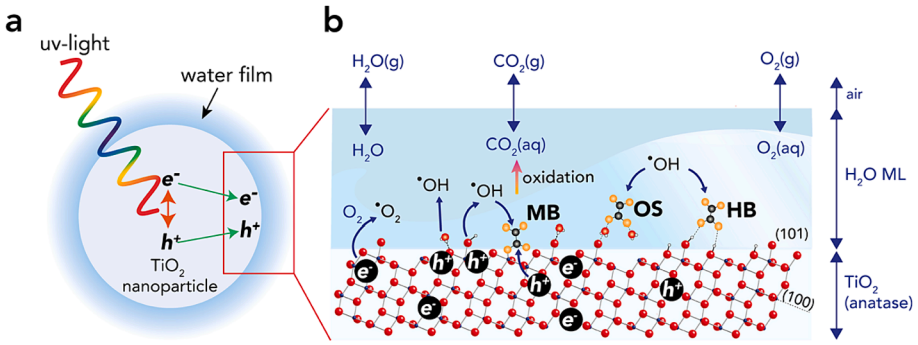

Fig. 1. Schematic representation of TiO_2 photoexcitation producing $^{\bullet}OH$ radicals in thin water films, and subsequent scavenging by oxalate. (a) Light activates charge separation in the TiO_2 bulk. While these charged carriers migrate from the bulk to the surface, they can be trapped and recombined. (b) Charges that are not trapped and/or recombined reach the surface and react with adsorbed (metal-bonded (MB), hydrogen-bonded (HB), and outer-sphere (OS)) species. Holes oxidize water film molecules and TiO_2 surface hydroxyl groups, producing hydroxyl radicals ($^{\bullet}OH$). Electrons combine with molecular oxygen through a series of reduction, protonation, and disproportionation reaction to generate reactive oxidative species (ROS, *e.g.*, $O_2^{\bullet-}$/$HO_2^{\bullet}$, H_2O_2, $^{\bullet}OH$). These radicals react with adsorbed oxalate (electron donor) of different binding modes (MB and OS/HB), to produce CO_2 as a final product.

(OS, with intervening water molecules) complexes (Fig. 1 b).[40,41] Uncertainties however remain regarding to the decomposition mechanisms, including whether water films can promote or inhibit TiO_2 photoreactivity.[29–36].

To advance our knowledge of water film-driven photocatalysis, we resolved the water film-mediated photodecomposition of a dicarboxylate ligand, oxalate (OX), bound to TiO_2 nanoparticles. Oxalate is an abundant low-molecular weight organic compounds in atmospheric aerosols [42] and soil systems.[43] It is also a contaminant from industrial activities, such in as alumina production [44] and metallurgy. [45] Focusing on the photo-reactivity of oxalate on TiO_2 is consequently relevant for environmental problems, as well as making new fundamental chemistry accessible for study.

Previous solution-based work showed that oxalate and oxalic acid are easily decomposed by photo-activated TiO_2 to CO_2 or (bi)carbonates.[46] This can be understood by the low reduction potential of $CO_2(g)/H_2C_2O_4(aq)$ (–0.49 V *vs* standard hydrogen electrode). Photodegradation rates of oxalate were also shown to be larger at pH values below the isoelectric point of TiO_2 (pH 5.6–6).[47] This can be understood by vibrational spectroscopy work showing a dominance of MB oxalate surface complexes under acidic conditions, [48–50] namely where the surface is positively charged.[20] Under these conditions, oxalic acid decomposition to $CO_2(g)$ by TiO_2 follows a Langmuir-Hindshelwood mechanism, one that involves two adsorbed species. [51] Other studies [50,52,53] also suggested that readsorption during irradiation changed the configuration of oxalate on TiO_2, a mechanism that, in turn, modified photodecomposition mechanisms.[54] Oxalate was, additionally, studied as an effective hole scavenger in the photocatalytic degradation of pharmaceutical pollutants by TiO_2 under visible light.[55]

In this work, we offer new insight into the photocatalytic decomposition of TiO_2-bound oxalate driven by nanometric water films, formed under atmospherically relevant conditions. This work fills the gaps between efforts in high-vacuum and aqueous systems, and gas-phase based TiO_2 photocatalysis. Using vibrational spectroscopy, we demonstrate that variations in water film thickness drove contrasting mechanisms on oxalate photodecomposition rates and yields under O_2-bearing and O_2-free environments. Our findings have direct implications for understanding water film-driven photocatalytic reactions that are important to terrestrial environments (*e.g.,* vadose zones of soils), atmospheric chemistry (*e.g.*, aerosol composition) and technology (*e.g.,* indoor air treatment).

2. Experimental Section

2.1. Material characterization

Commercial TiO_2 (Aldrich, No. 718467) with properties similar to the well-studied commercial P25 Degussa (Evonik) [56,57] was used to study oxalate degradation in thin water films. These particles consist of a physico-chemical mixture of 90 % anatase and 10 % rutile, [56] as determined by powder X-ray diffraction (XRD, PANalytical X'Pert^3, *Supporting Information*, Fig. S1). Scanning and transmission electron microscopy (SEM/TEM, Fig. S1) revealed a homogeneous distribution of 21 ± 6 nm sphere-like or cuboid particles exposing dominant (1 0 1), (1 0 0), (0 0 1) and (0 1 0) surfaces.[57,58] A 91-point $N_2(g)$ adsorption/desorption isotherm (Micromeritics TriStar 3000) gave a B.E.T. specific surface area [59] of 53 m^2/g. X-ray photoelectron spectroscopy (XPS, Kratos Axis Ultra) showed a surface composition of Ti:O:OH = 1:2.1:0.17 (*Supporting Information*, Table S1), indicating the presence of Ti vacancies and non-stoichiometric surface OH groups. Furthermore, XPS confirmed that all surface Ti sites were Ti(IV). Details on all characterization methods are accessible in *Supporting Information*. All experiments were performed on this TiO_2 sample without any further treatment.

2.2. Adsorption experiments and chromatography analyses of solutions

Oxalate was adsorbed in aqueous suspensions of TiO_2 nanoparticles under $N_2(g)$. Experiments were performed in 15-mL Falcon® tubes covered by aluminum foil to avoid exposure to light. MilliQ water was used for preparing all solutions. A 0.5 mL aliquot of an aqueous suspension of 20 g/L TiO_2 was mixed with 9.5 mL of 0.5 mM oxalic acid solution (>99.5 %, Scharlau) under $N_2(g)$, achieving a total oxalate concentration ($[OX]_{tot}$) of 47.5 mM per g TiO_2. This amounts to a total concentration of ~ 5.4 oxalate molecules per nm^2 TiO_2 (OX/nm^2). Small aliquots of 1 M HCl (Merck) and 1 M NaOH (Merck) were used to adjust the suspension pH to ~ 3.2, resulting in ionic strength values of ~ 1 mM. The resulting suspensions were then equilibrated using an end-to-end rotator for 24 h before they were centrifuged at 2900 g for 15 min. The supernatants were thereafter collected by filtration using a 0.2-μm filter, and their final oxalate concentration analyzed by ion chromatography (IC).

The IC system consisted of a modified liquid chromatography instrument (LC-10AD, Shimadzu), an anion separation column (Metrosep A Supp 5–150/4.0, Metrohm), a suppressor system equipped with a suppressor membrane (Xenoic® XAMS, Diduco AB) and a generation pump (Xenoic® ASUREX-A100, Diduco AB), and a conductivity detector (prototype, no brand) to detect ions. The mobile phase was a carbonate

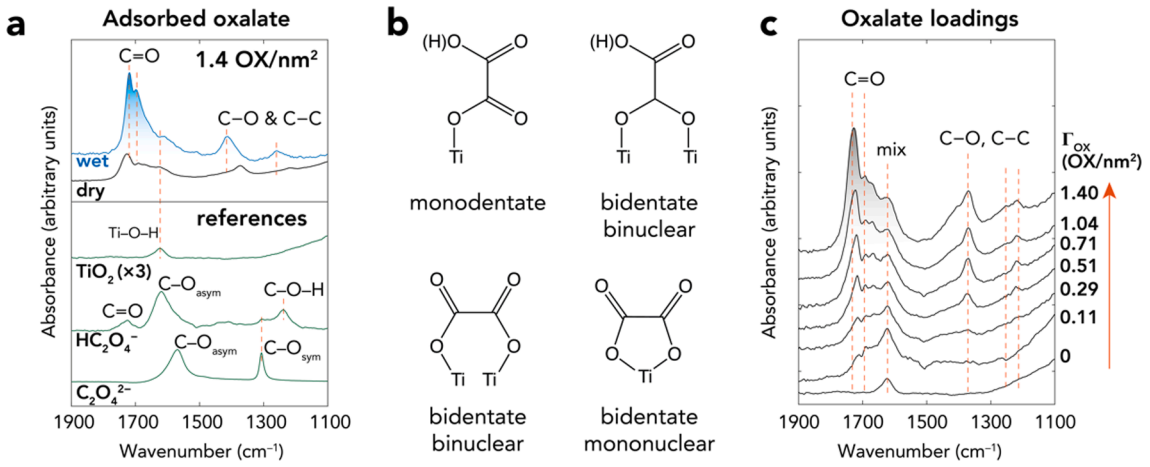

Fig. 2. Oxalate binding on TiO_2 nanoparticles. (a) ATR-FTIR spectra of wet (blue) and N_2-dry (black) films of TiO_2 with oxalate loadings of 1.4 OX/nm^2, and ATR-FTIR of references (green): dry TiO_2 film, $HC_2O_4^-$ ions and $C_2O_4^{2-}$ ions. The spectrum of the wet TiO_2-oxalate film was obtained on the centrifuged wet paste deposited on ATR surfaces, and the spectrum of the film was taken after this wet paste was dried under N_2(g) (c.f. Section 2.4). The spectra of $HC_2O_4^-$ ions and $C_2O_4^{2-}$ ions were obtained from 100 mM oxalate solutions at pH 3.3 and at pH 6, respectively. Contributions from the bending region of liquid water were subtracted from the spectrum of the wet TiO_2 film and of the two oxalate solutions. To obtain the pure spectrum of $HC_2O_4^-$ ions, contributions of the $C_2O_4^{2-}$ ion in the oxalic acid solution were subtracted. Both spectra (dry, wet) were scaled for the absorbance of an oxalate-free dry TiO_2 solid (reference TiO_2, below) at 600 cm^{-1}. The spectra of $HC_2O_4^-$ and $C_2O_4^{2-}$ ions were not scaled. (b) Possible surface metal-bonded (MB) complexes of oxalate on TiO_2 anatase surfaces according to previous studies.[48,50] These complexes can be either protonated or deprotonated. (c) ATR-FTIR spectra of N_2-dry films of TiO_2 with oxalate loadings varied from 0 to 1.4 OX/nm^2, revealing an increase in loading of oxalate surface complexes. All spectra were scaled with respect to IR absorbance at 600 cm^{-1}. (For interpretation of the references to colour in this figure legend, the reader is referred to the web version of this article.)

buffer solution (8 mM Na_2CO_3/2.5 mM $NaHCO_3$, Merck) to eluate oxalate ions in the separation column. Elution was performed at flow rate of 0.7 mL/min under a total pressure of 78 bars.

2.3. Water loadings by microgravimetry

Water loadings acquired on initially dried pure (unreacted) TiO_2 and TiO_2-oxalate samples were determined by dynamic vapor sorption (DVS), using a DVS Advantage ET 2 instrument (Surface Measurement Systems). These were acquired through a 21-point adsorption/desorption isotherm cycle between 0 and 90 % Relative Humidity (RH) (0.0095–2.84 kPa H_2O) at 25 °C. Measurements were made using ~ 30–60 mg samples initially dried at ~ 0 % RH (25 °C) for 10 h to remove adsorbed water from ambient atmosphere. The equilibrium criteria for each preselected RH step were 60 min for steps between 10 and 60 % RH, but 180 min for steps between 70 and 90 % RH. Gravimetric measurements were continuously taken every 1 min, and a complete adsorption − desorption isotherm cycle took up to 48 h. Using the B.E.T. specific surface area of TiO_2, the gravimetrically-determined water loadings were expressed in terms of H_2O/nm^2. These values were, in turn, expressed in terms of monolayer (ML), assuming that 1 ML is equivalent to 12 H_2O/nm^2. This value is more typical of water films adsorbed to (hydr)oxo-terminated metal oxide surfaces.[60–62]

2.4. Vibrational spectroscopy

Vibrational spectra were collected on a Fourier Transform Infrared (FTIR) spectrometer (Bruker Vertex 70/V) using an Attenuated Total Reflectance (ATR, diamond-bound Golden Gate® GS10563, Specac) accessory in a room kept at 25 ± 1 °C. The instrument was equipped with a deuterated L-alanine doped triglycine sulfate (DLaTGS) detector. Measurements were carried out in the 600–4500 cm^{-1} range at a resolution of 4 cm^{-1} and at forward/reverse scanning rate of 10 kHz, and the signals were treated with a Blackman-Harris 3-term apodization function with 16 cm^{-1} phase resolution and the Mertz phase correction algorithm. Each spectrum was obtained by coadding 100 spectra for collected over a ~ 89 s period.

Prior to all experiments, an aliquot (5–10 μL) of the pre-equilibrated TiO_2-oxalate wet paste was deposited on the diamond window of the ATR. It was then dried for 1 h under a flow of dry N_2(g) (~ 0% RH, 0.0095 kPa H_2O) in a closed-loop flow-through cell. FTIR spectra were continually recorded during this process to ensure that the samples were completely dried. This was confirmed by the loss of liquid water bending (~ 1640 cm^{-1}) and stretching (~ 3400 cm^{-1}) modes. This dry solid state TiO_2-oxalate film was then used for the following experiments.

2.4.1. Water vapor adsorption in the dark

A water adsorption/desorption isotherm cycle was carried out on the initially dry TiO_2-oxalate solid state film exposed under 500 mL flow of humidified N_2 (g) (0 to 90 % RH, corresponding to 0.0095 to 2.84 kPa H_2O at 25 °C) in the dark. Relative humidity was controlled using a humidity generator module (MHG32, proUmid). FTIR spectra were continuously collected during the experiments.

2.4.2. Photo-oxidation experiments

Photoreactions were performed under a 500 mL flow of oxygen-rich air (N_2:O_2 = 80:20 % p/p and CO_2 of ~ 300 ppm) and oxygen-free N_2(g). Initially the N_2(g) dried TiO_2-oxalate dried film was equilibrated with either one of these two gas compositions at a preselected humidity (0, 10, 30, 50, 70 and 90 % RH, controlled by MHG32) at 25 °C for 1 h in the dark. This procedure was used to ensure for water film stability. The samples were then irradiated using 150 W Xe arc lamp (broad UV–visible spectrum covering 200–1000 nm, LSH102, Quantum Design GmBH) through an optical fiber (fused silica, LSZ152, Quantum Design GmBH) connected at a 45° angle into the closed-loop flow-through cell. Although this irradiation angle was not optimized for maximal irradiance flux, it was still sufficient to provide 25 mW/cm^2 photon energy on the 2 × 2 mm^2 area of the sample. Photo-oxidation experiments were carried out for minimum of 20 h, and FTIR spectra were collected continuously during all experiments. We note that the temperature of the ATR cell did not increase by more than 1 °C over a 8-h irradiation period. It is thereby unlikely that hikes in light-induced temperatures affected oxalate decomposition.

2.4.3. Gaussian deconvolution and kinetic modeling

The 1500–1850 cm^{-1} region was modeled using a linear

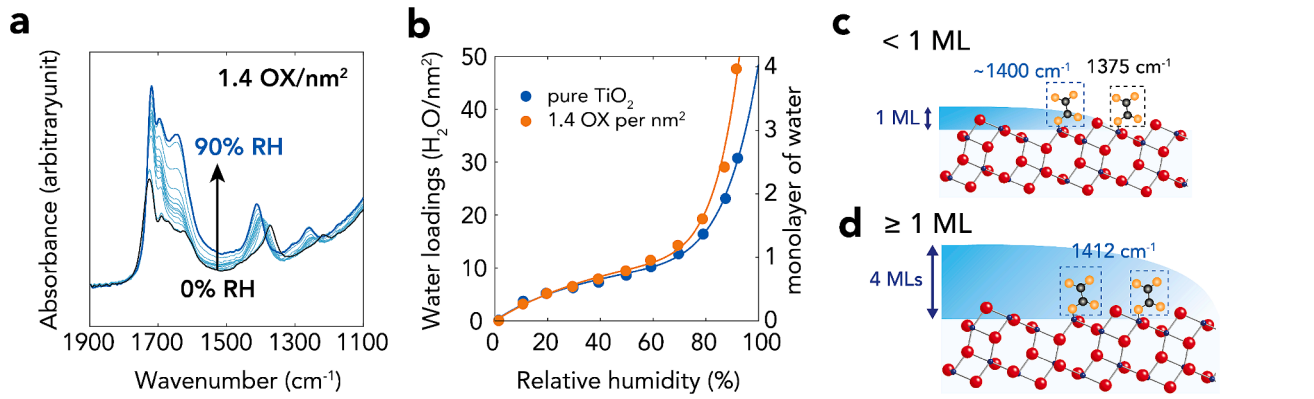

Fig. 3. Response of adsorbed oxalate to water films in the absence of light. (a) FTIR spectra of 1.4 OX/nm^2 on TiO_2 exposed to humidity from 0 to 90 % RH. Spectra show that water bending (~ 1640 cm^{-1}) and oxalate bands concurrently increased in intensity. Moreover, the oxalate C–O/C–C band pair progressively shifted in position (1412 to 1375 cm^{-1}, and 1261 to 1219 cm^{-1}) upon exposure to water vapor, as a result of hydration. (b) Microgravimetry revealed that 1 monolayer (ML) water film formed on the oxalate-free ("pure TiO_2") and oxalate-bearing ("1.4 OX/nm^2") TiO_2 at 70 % RH, and that films grew up to ~ 4 MLs at 90 % RH. (c-d) Schematic presentation of (c) partially hydrated TiO_2 and bound oxalate in sub-monolayer (< 1 ML) water coverages, and (d) fully hydrated TiO_2 and oxalate species in thicker water films (≥ 1 ML). Hydration shifted and enhanced the vibrational absorbances of oxalate bands in (a).

combination of Gaussian components:

$$A(\nu) = \sum_{1}^{n} A_{n,max} e^{-(\nu-\nu_n)^2/(2\sigma_n^2)} \quad (1)$$

with the maximal absorbance ($A_{n,\max}$) of the n^{th} component centered at wavenumber ν_n, and with the width of the distribution $\sigma_n$ethod for our study as attempts using multivariate methods [63] were unsuccessful in clearly discerning the evolution of different bands over reaction time. Spectral deconvolution was performed in a sequence of time-resolved spectra with absorbance values offset to 0 at 1850 cm^{-1}, followed by normalization of all absorbance values to that of the Ti–O bonds at 600 cm^{-1} to account for differences in sample mass in different experiments, and baseline correction using a simple linear function. All Gaussian and kinetic parameter optimization (non-linear least square) calculations were performed with MATLAB (version R2021b, The Mathworks, Inc.).

3. Results and discussion

Resolving the film-driven photocatalytic decomposition of oxalate on TiO_2 using vibrational spectroscopy first requires knowledge of the spectral signatures of bound oxalate species and their response to variations in hydration. To this end, we begin this study by presenting the chief vibrational markers of bound oxalate in the dark. These markers were then used to resolve how variations in water film thickness and dissolved oxygen impacted oxalate photodecomposition rates, efficiency and products.

3.1. Oxalate binding on TiO_2 in the dark

Equilibrating aqueous suspensions of TiO_2 with $[OX]_{tot}$ = 47.5 mM/g TiO_2 at pH 3 in the dark for 24 h adsorbed ~ 1.4 OX/nm^2. This loading was lower than the total O site density (*e.g.*, ~15 O/nm^2 on the (1 0 1) plane of anatase), [23] and the population of non-stochiometric surface OH groups (~5 OH/nm^2) [64]. From an additional adsorption isotherm (Fig. S2), we also find that this loading was close to the maximal value (1.44 OX/nm^2) that can be achieved on the TiO_2 used for this study. This aligns with other previous efforts [65] on a similar type of TiO_2.

3.1.1. Vibrational signatures of bound oxalate

Attenuated Total Reflectance-Fourier Transform Infrared (ATR-FTIR) spectra (Fig. 2 a) of wet centrifuged TiO_2 pastes revealed bands characteristic of metal-bonded (MB) species, in accordance with previous work.[48,49] This can be appreciated by the oxalate C = O stretching (~ 1718 and ~ 1690 cm^{-1}), C–O or C–C stretching and even the O–C = O bending (1412 and 1261 cm^{-1}) frequencies, which were shifted in relation to the dominant solution $HC_2O_4^-$ species [48,49,66] (Fig. 2 a). Previous suggestions for MB species [50,54] include those of Fig. 2 b. Because oxalate forms these very strong MB species on TiO_2 under acidic conditions (pH < pH_{iep} ~ 6.5, [47] Fig. S3), outer-sphere complexes (OS) or hydrogen-bonded (HB) species [67] were of comparatively low loadings. Furthermore, previous studies [49,66,68] reported that these OS and HB species have similar spectral profiles to the one of the free $C_2O_4^{2-}$ ion (Fig. 2 a). In short, they can display bands at ~ 1560–1600 cm^{-1}, which possibly overlapped with surface Ti–O–H bending modes (1624 cm^{-1}; Fig. 2 c), as well as bands at ~ 1300 cm^{-1} which were below the detection limit.

Removing water from the wet TiO_2 paste, using a stream of N_2(g), decreased the intensities of all bands, and especially the intensity ratio between the C = O and C–O/C–C band pair. It shifted the C–O/C–C band pair to lower wavenumbers ($\Delta\nu$ = ~ 40–45 cm^{-1}, 1412 to 1375 cm^{-1} and 1261 to 1219 cm^{-1}), yet it did not greatly affect C = O band positions (1718 to 1724 cm^{-1}). We interpret this to the loss of hydration water molecules, which shifted the C–O bond strength in the water films.

We also investigated the effects of oxalate loadings (Fig. 2 c) on possible loading-dependent spectral responses during photocatalytic decomposition experiments. These experiments showed that band intensities scaled with oxalate loadings, and that bands were not shifted. The 1690 cm^{-1} band became, however, more intense than the 1724 cm^{-1} band at oxalate loadings below 0.5 OX/nm^2. In accordance with previous work [48–50,54], we interpret this as evidence that a distinct MB species [69] (MB1) was preferentially expressed at 1724 cm^{-1} and that a second complex (MB2) was dominant at 1690 cm^{-1}. These strongly adsorbed species may possibly include those that preferentially bind on the more reactive (0 0 1) plane of anatase, yet the spectral profiles were not sufficiently informative to assign these bands to distinct coordination environments (Fig. 2b).[23] Still, we can foresee that variations in loadings could impact MB1/MB2 speciation and, in turn, photocatalytic efficiency.[54]

Exposing these dry oxalate-bearing TiO_2 films to water vapor (10–90 % RH) formed water films, which can be seen by FTIR through the growth of O–H stretching (3400–3200 cm^{-1}, Fig. S4) and water bending (~ 1640 cm^{-1}, Fig. 3 a) bands. Spectra of the O–H stretching region (Fig. S4) also revealed free O–H groups (~ 3700 cm^{-1}) from water molecules which were presumably either directly bound to Ti^{4+} sites (*e.g.*, on the (1 0 0) face) as similar to previous study [60] on water films forming on iron oxides, or from the topmost surface region (*i.e.* air/water interface) of the water films.[70] From microgravimetry (Fig. 3b),

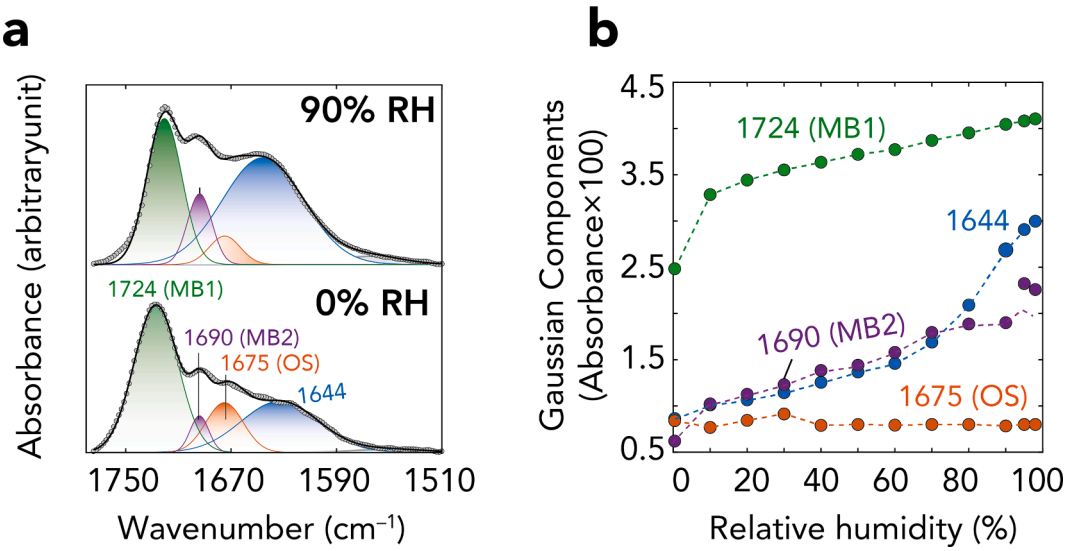

Fig. 4. Gaussian deconvolution of the 1510–1780 cm^{-1} in TiO_2 equilibrated with 1.4 OX/nm^2. (a) Example of deconvolution of sample exposed to 0 and 90 % RH in the absence of light for 20 h, here revealing four components. (b) Gaussian component intensities, showing congruent growth of the C = O stretching of MB1 (1724 cm^{-1}) and MB2 (1690 cm^{-1}) complexes and water bending (1644 cm^{-1}) bands with humidity. The C = O component of OS complexes (1675 cm^{-1}) remained unchanged regardless of water loadings.

we find that films of less than monolayer (1 ML, ~ 12 H_2O/nm^2) formed below 70 % RH, and of up to 4 MLs (~ 48 H_2O/nm^2) at 90 % RH (Fig. 3 b). Also, microgravimetry retrieved similar masses of the dry sample before (57.470 ± 0.001 mg) and after (57.541 ± 0.006 mg) adsorption, a result indicating that no oxalate was evaporated or lost due to water adsorption. Hydration progressively and systematically enhanced the intensities and shifted position of the oxalate C–O/C–C band pair back to the positions (1412 cm^{-1} and 1261 cm^{-1}) of the wet pastes. Additionally, because the positions of the C = O stretching band were not greatly changed, while their intensities enhanced by water loadings, we can infer that sub-monolayer coverages (< 70 % RH, Fig. 3 b) preferentially hydrated bound oxalate surface complexes (Fig. 3 c). Thicker water films (≥ 1 ML), on the other hand, developed full hydration shells on all bound oxalate (Fig. 3 d), and thus generated similar spectroscopic responses to those of the wet pastes (Fig. 2a). These spectroscopic responses were therefore not related to competitive adsorption of water to oxalate. By comparing the IR spectra of dry TiO_2-oxalate film before and after water vapor adsorption (Fig. S4), and combining with microgravimetry (as described earlier), we conclude that there was no evidence showing that oxalate was desorbed from the water films. This conclusion is also supported by noting that (1) the available reactive crystalline oxygen site density (12.5 O/nm^2) [71] is ~ 1 order of magnitude larger than oxalate loadings (1.4 OX/nm^2), and (2) the volume of water in 4 ML-thick water films was substantially smaller than in the solutions in which the adsorption experiments were performed (15 mL, cf. Section 2.2).

3.1.2. *Spectral components of bound oxalate species*

To gain further insight into the complexation modes of oxalate and their response to hydration, we resolved the 1510–1780 cm^{-1} region into four Gaussian components (Fig. 4 a). This revealed (i) the dominant 1724 cm^{-1} 'MB1' component (C = O stretch), (ii) A less dominant 'MB2' component at 1690 cm^{-1} (C = O stretch) [69], (iii) an even less dominant oxalate component at 1675 cm^{-1} (OS), and finally (iv) a component

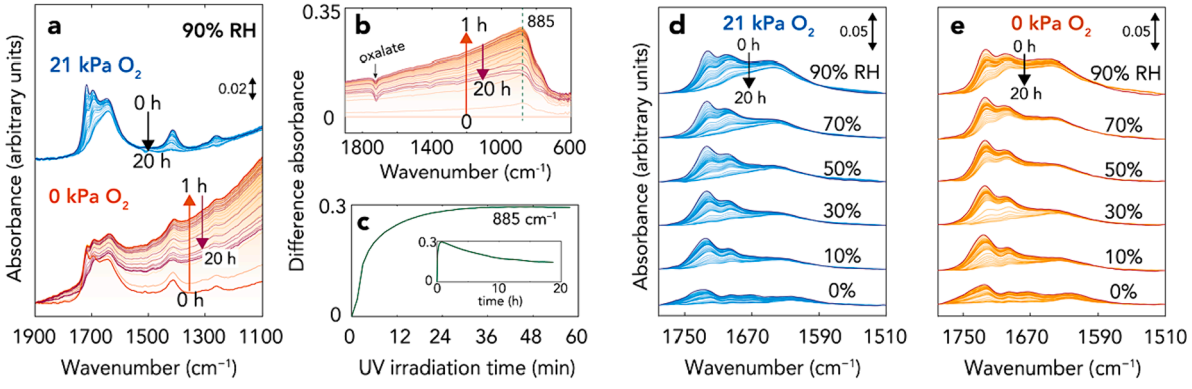

Fig. 5. FTIR spectral evidence for humidity- and oxygen-dependent photocatalytic (broad UV–vis 200–1000 nm, 25 mW/cm^2) decomposition of bound oxalate (1.4 OX/nm^2) on TiO_2. Reactions were conducted in (a,d) oxygen-rich (21 kPa O_2), and (a,e) oxygen-free atmospheres for 20 h. (a, top) Time-resolved spectra for reactions under 21 kPa O_2 and 90 % RH revealed a decrease in oxalate loadings through the loss of all oxalate bands. (a, bottom) Spectra of experiments under oxygen-free N_2(g) and 90 % RH revealed background changes caused by irradiation, alongside with the loss of oxalate bands. (b) The background increase in (a, bottom) results from the broad 885 cm^{-1} band of shallow trap electrons (STIRA) within first ~ 60 min (c), which then slowly decayed for the rest of the irradiation period (inset in c and cf. Fig. 6 & S9). This band was revealed by taking the difference spectra from the raw data in (a, bottom). (d,e) Baseline-subtracted spectra showing comparable humidity-dependent losses of oxalate bands under (d) O_2-rich and (e) O_2-free conditions. Difference spectra showing the 885 cm^{-1} in all O_2-free experiments are accessible in Supporting Information, Fig. S9.

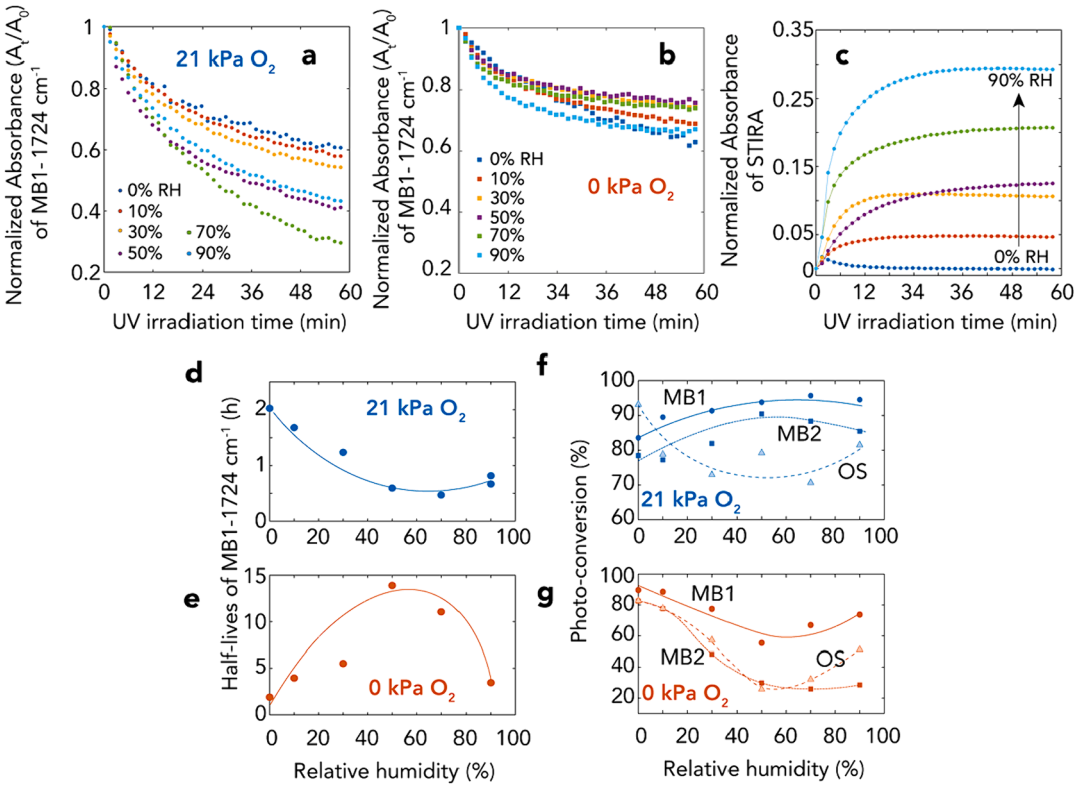

Fig. 6. Time-dependent absorbances revealing oxalate photodecomposition. (a,b) Normalized Gaussian component absorbances (A_t/A_0; Eqn. (13) of the C = O band of MB1 (1724 cm^{-1}) during photoreactions over 60 min periods (cf. Fig. S10 for entire 20 h period) under (a) O_2-bearing (21 kPa O_2) and (b) O_2-free (0 kPa O_2) atmospheres over a range of humidity (0–90 % RH). (c) Time-dependent STIRAs (885 cm^{-1} band) for the first 60 min of the reaction (cf. Fig. S9 for entire 20 h period). (d,e) Reaction half-lives of MB1 and (f,g) percent of photoconversion after a 20 h period, derived from the data in (a,b) for MB1 and in Fig. S10 for MB2 and OS.

at 1644 ± 3 cm^{-1} from overlapping contributions of Ti–O–H bending, water bending, and unresolved oxalate species. D_2O exchange (Fig. S5) displaced the water band and the Ti–O–H band but left a small oxalate component. Deconvolution also successfully separated contributions of the water and OH-related bending mode at ~ 1644 cm^{-1} from the components at 1690 and 1675 cm^{-1} at elevated humidity (Fig. 4 a,b). This operation will become useful for teasing out unwanted contributions generated from the photodecomposition at lower oxalate loadings (Fig. S6).

While the band intensities of the MB1 and MB2 species scaled with humidity, those of another oxalate component (1675 cm^{-1}) did not respond (Fig. 4 b & S6). One possibility is that this species retained its full hydration environment. For this reason, we assigned this component to a hydrated OS complex, an interpretation that could possibly explain previous work.[49] Additionally, from the total Gaussian absorbances, we estimate that total oxalate loadings of 1.4 OX/nm^2 were 63 % MB1, 16 % MB2, and 21 % OS species.

3.2. Oxygen- and humidity-dependent photoreactions

Using these spectroscopic markers for oxalate speciation, we resolved photodecomposition reactions as oxalate-bearing TiO_2 nanoparticles were exposed to a broad spectrum (200–1000 nm) of UV–visible light over time. Photo-experiments in this study will be explored in O_2-bearing and O_2-free sub-monolayer to multilayered water films (Figs. 5 and 6) to uncover how these conditions impacted the fate of oxalate.

3.2.1. Oxygen-dependent photoreactions

The vibrational spectra revealed that exposing 4-ML water films (90 % RH) to 21 kPa O_2 and UV light triggered photodecomposition reactions, detected through the loss of oxalate bands (Fig. 5a). No major band shifts occurred during the entire 20 h of the reaction, indicating that photodecomposition did not generate intermediate products (*e.g.*, formic acid), as previously shown.[44,53] This situation thus contrasts with experiments in a liquid cell under flow-through conditions [53] where species re-adsorbed on TiO_2 contributed to oxalate bands growth during irradiation. Comparing these spectra with those of lower oxalate loadings under hydration (0–90 % RH, no light, Fig. 2c & S6) confirmed that the spectral response was still from oxalate.

These results consequently support the interpretation that the photodecomposition of oxalate MB complexes producing CO_2 in multilayer water films begins with the well-known [72] production of $^{\bullet}OH$ radicals. These reactions begin with:

$$TiO_2 + \text{light} \rightarrow e^- + h^+ \quad (2)$$

then proceed through surface hydroxo groups:

$$\equiv Ti^{IV}\text{–}OH + h^+ \rightarrow \equiv Ti^{IV}\text{–}{}^{\bullet}OH^+ \quad (3a)$$

or chemisorbed water:

$$\equiv Ti^{IV}\text{–}OH_2^+ + h^+ \rightarrow \equiv Ti^{IV}\text{–}{}^{\bullet}OH^+ + H^+ \quad (3b)$$

These radicals could also desorb into the multilayered water films:

$$\equiv Ti^{IV}\text{–}{}^{\bullet}OH^+ \rightarrow \equiv Ti^{IV} + {}^{\bullet}OH\ (aq) \quad (4)$$

where they could, in turn, drive solvent-hosted reactions.

Both hole and the $^{\bullet}OH$ radical can oxidize adsorbed oxalate (*e.g.*, $\equiv Ti^{IV}\text{–}C_2O_4^{2-}$) via [44]:

$$\equiv Ti^{IV}\text{–}C_2O_4^{2-} + h^+ \rightarrow \equiv Ti^{IV}\text{–}C_2O_4^- \quad (5)$$

$$\equiv Ti^{IV}\text{–}C_2O_4^- + {}^{\bullet}OH + H^+ \rightarrow \equiv Ti^{IV} + 2CO_2 + H_2O \quad (6)$$

thus regenerating the reactive $\equiv Ti^{IV}$ sites after CO_2 generation.

Of note, the presence of oxygen plays an important role as an electron scavenger, and generates a variety of (adsorbed) ROS species through [72]:

$$O_2 + e^- \rightarrow O_2^{\bullet-} \quad (7)$$

$$O_2^{\bullet-} + H^+ \rightarrow HO_2^{\bullet} \quad (8)$$

$$O_2^{\bullet-} + 2H^+ + e^- \rightarrow H_2O_2 \quad (9)$$

$$H_2O_2 + e^- \rightarrow {}^{\bullet}OH + OH^- \quad (10)$$

These ROS can, in turn, oxidize adsorbed oxalate, for example, through [44]:

$$\equiv Ti^{IV}\text{–}C_2O_4^- + HO_2^{\bullet} \rightarrow \equiv Ti^{IV}\text{–}CO_3^- + HCO_3^{\bullet} \quad (11)$$

as we foresee that $HO_2^{\bullet}$ should be the dominant species in the acidic water films considered in this work ($O_2^{\bullet-}$/ $HO_2^{\bullet}$, pKa = 4.8). We also note that ROS can decrease the rate of electron-hole recombination.[72]

Reactions in the absence of O_2 (Fig. 5a) generated, in contrast, a baseline increase peaking at 885 cm^{-1} (Fig. 5b,c) over the course of the first ~ 30 min of irradiation. The baseline then decayed over the rest of the reaction period (Fig. 5b,c). We attribute this baseline to a Shallow Trap IR Absorbance (STIRA).[73] The origin of the STIRA is attributed to variations in Ti–O bond strengths in the surface and in the bulk, which are caused by the reduction of Ti^{IV} sites through:

$$Ti^{IV}\text{–}O^- + e^- \rightarrow Ti^{III}\text{–}O^- \quad (12)$$

as well as by charge-compensating protonation reactions of the type [73,74]:

$$Ti^{III}\text{–}O^- + H^+ \rightarrow Ti^{III}\text{–}OH \quad (13)$$

The latter reaction is facilitated in proton-rich samples, such as those considered for this work.

We take the subsequent decay of the STIRA during irradiation as an indication that trapped electrons ultimately recombined with holes:

$$Ti^{III}\text{–}OH + h^+ \rightarrow Ti^{IV}\text{–}O^- + H^+ \quad (14)$$

From the time-resolved STIRA (inset of Fig. 5c, S9), this recombination can take place over the course of at least 19 h.

3.2.2. Humidity-dependent photoreactions

To test the water film thickness dependence on photoreaction yields, we performed another set of experiments at 10–90 % RH, again in the presence (Fig. 5d & S8) and in the absence of oxygen (Fig. 5e & S8). To compare the spectral response of oxalate in the presence and absence of O_2, we extracted all STIRA-generated baselines (Fig. S7) from the spectra.

These experiments revealed that water film thickness played (i) no strong effects in O_2-bearing but (ii) important effects in O_2-free systems. Also, from the intensities of the 1724 cm^{-1} bands after 20 h of irradiation (Fig. 5d & S8), we find that O_2-bearing films decomposed ~ 80–90 % of the oxalate, irrespective of film thickness. On the other hand, while this level of photodecomposition was also achieved in the absence of O_2 on dry TiO_2 (Fig. 5e & S8) and in sub-ML water films (10–30 % RH), thicker films formed at and above 50 % RH decomposed only ~ 30–50 % of the oxalate.

3.3. Kinetics of photoreactions

The time-dependent intensities of the Gaussian components were used to gain insight into the kinetics of the photocatalytic decomposition reactions for oxalate (Fig. 6a,b), and to track the STIRAs (Fig. 6c). Preliminary analyses on the MB1 (1724 cm^{-1}) and the C–O/C–C band pair (Fig. S10) revealed highly comparable responses. Because we could not extract other contributions of the 1690/1675 cm^{-1} pair from the C–O/C–C bands, we focused our analyses on three dominant components of the C = O stretching region (1724, 1690 and 1675 cm^{-1}). Furthermore, because absorbances of the 1724 and 1690 cm^{-1} scaled with humidity (Fig. 4 b), we normalized their absorbances to those at the onset of the reaction (A_0) at each humidity (Fig. 6 a,b & S10).

Kinetic modeling of these time-dependent values (A_t/A_0) showed that the reactions did not follow a simple first order kinetic (Fig. S11). As a result, we focused our discussion on the time-resolve absorbance profiles of these bands, as well as their half-lives (Fig. 6 d,e; A_t/A_0= ½ from Fig. 6a,b), as they can still provide insights into reaction kinetics. We also derive photoreaction yields (Fig. 6 f,g) from these absorbance profiles. We begin our discussion on the dominant MB1 (1724 cm^{-1}) as it represented ~ 63 % of total oxalate that undergone humidity-dependent photodecomposition in the presence and absence of O_2. We thereafter highlight the influence of complexation modes of oxalate on photocatalytic efficiency in water films.

3.3.1. O_2-rich water films

To tease out the specific contributions of water on the photoreactions, we begin by highlighting the intrinsic properties of dry TiO_2 on the photodecomposition of oxalate. Photoreactions in the absence of water (0 ML, 0 % RH) in 21 kPa O_2 effectively decomposed ~ 80 % of the bound oxalate after 20 h, and with a half-life of ~ 3 h (Fig. 6d). We explain this high photodecomposition yield by direct hole transfer (HT) from TiO_2 to the bound oxalate:

$$\equiv Ti^{IV}\text{–}C_2O_4^{2-} + h^+ \rightarrow \equiv Ti^{IV}\text{–}C_2O_4^- \quad (15)$$

$$\equiv Ti^{IV}\text{–}C_2O_4^- + 2\,h^+ \rightarrow \equiv Ti^{IV}\text{–}C_2O_4^{\bullet+} \quad (16)$$

$$\equiv Ti^{IV}\text{–}C_2O_4^{\bullet+} \rightarrow \equiv Ti^{IV}\text{–}CO_2^{\bullet+} + CO_2 \quad (17)$$

$$\equiv Ti^{IV}\text{–}CO_2^{\bullet+} + O_2^{\bullet-} \rightarrow \equiv Ti^{IV} + CO_2 + O_2 \quad (18)$$

Note that superoxide ($O_2^{\bullet-}$) in Eq.18 is a result of direct reduction of oxygen via Eq. (7). Additionally, irradiation of TiO_2 bound oxalate facilitated electron transfer from oxalate to the TiO_2 conduction band through ligand-to-metal charge transfer (LMCT) and generated CB electrons (e^-) and the oxalate radical anion ($C_2O_4^{\bullet-}$). The $C_2O_4^{\bullet-}$ radical anion then spontaneously decomposed into CO_2 and a $CO_2^{\bullet-}$ radical anion, which in turn reacted with oxygen:

$$\equiv Ti^{IV}\text{–}C_2O_4^{2-} \rightarrow \equiv Ti^{III}\text{–}C_2O_4^{\bullet-} \quad (19)$$

$$\equiv Ti^{III}\text{–}C_2O_4^{\bullet-} \rightarrow \equiv Ti^{III}\text{–}CO_2^{\bullet-} + CO_2 \quad (20)$$

$$\equiv Ti^{III}\text{–}CO_2^{\bullet-} + 2O_2 \rightarrow \equiv Ti^{IV} + CO_2 + 2O_2^{\bullet-} \quad (21)$$

The generated $O_2^{\bullet-}$ can then proceed through Eqs. (8)–(10).

Photoreaction yields (Fig. 6 f) directly scaled with humidity, increasing from ~ 80 % conversion at 0 % RH to full decomposition at 70 % RH (1 ML), and then reversing back to ~ 80 % conversion at 90 % RH (4 MLs). Reaction half-lives (Fig. 6 d) mirrored this trend by decreasing, in turn, from ~ 120 min down to ~ 28 min at 70 % RH and slightly increasing to ~ 36 min at 90 % RH. In addition to the HT/LCMT processes and superoxide/hydroperoxyl radical production, we interpret the water loading-dependent trends in yield and half-life to arise from the water film-mediated production of $^{\bullet}OH$ radicals [72] in films of at least ~ 0.8 ML via Eqs. (3a) and (4).

It is thus this synergistic HT/LMCT, ROS production, and water-assisted $^{\bullet}OH$ radical production that explains the faster reaction rates (shorter half-lives) with water film loadings. Additionally, it is possible that the decreased acidity of thicker water films produced less H_2O_2, and therefore lowered $^{\bullet}OH$ radical concentrations (Eqs. (9)–(10)). This can consequently explain the minor reversal in trend at 90 % RH. Furthermore, because the diffusion of dissolved oxygen to TiO_2 surface is likely to be slower in thicker water films, it also can lower ROS production (Eqs. (7)–(10)) and consequently slow down oxalate photodecomposition.

3.3.2. O_2-free water films

Reactions in the absence of O_2 had contrasting humidity-dependent trends in half-lives (Fig. 6e) and reaction yields (Fig. 6g). Firstly, yields were on par with those of O_2-bearing films with up to 0.5 ML (30 % RH), but thereafter dramatically dropped in thicker films. Half-lives were, in contrast, comparable on dry TiO_2 (~ 2 h), then rose to ~ 15 h in the 0.8 ML (50 % RH) film, and dropped to ~ 3 h in 4 ML-thick films.

From the relatively constant and comparable rates in dry TiO_2 in the presence and absence of O_2, we propose that LMCT and HT were the chief mechanisms for oxalate photodecomposition. The hike in half-lives in O_2-free water films (10–90 % RH) signaled, on the other hand, that films could not sustain an important production of $^{\bullet}OH$ radicals compared to O_2-bearing films. We explain the drop in rates in O_2-free water films (10–90 % RH) using two primary processes: (i) the suppression of ROS, and (ii) faster charge recombination caused by the absence of electron-scavenging oxygen [19,72]. These effects nevertheless failed to account for the similar MB1 degradation rates in the presence (Fig. 6a) and absence (Fig. 6b) of O_2 in the first ~ 10 min of the reaction. These initially comparable rates can, however, be explained by the entrapment of electrons at Ti^{IV} sites (Eq. (12)), which gave rise to stable STIRAs (Fig. 6c and S9). Again, a STIRA signals the effective capture of electrons, thus enabling holes to migrate to the surface and oxidize oxalate through HT (Eqs. (15)–(18)) and/or generate $^{\bullet}OH$ (Eqs. (3)–(4)). However, within this context, the rates were rapid and comparable for only the first 10 min, and followed by a subsequent deceleration. We cannot explain this slow period by electron/hole recombination, as the existence of stable STIRAs (Fig. S9) during this period indicated that electron entrapment persisted, yet the holes were unable to effectively facilitate oxalate oxidation. Consequently, these findings suggest that recombination was not the key factor to slow down the photocatalytic rates in anerobic and hydrated conditions.

Another influential factor affecting photocatalytic rates and efficiency under anerobic conditions was the spatial confinement of electrons and holes. Previous modeling studies showed that hydration in aqueous solutions trapped electrons at surface Ti^{IV} sites, [38], and we can substantiate this through the STIRAs (Fig. 6c and S9) which we observed in the thicker, multilayered, water films. Additionally, based on recent work, [39] hydration could have rapidly localized holes at lattice/bulk O sites, a process that potentially decreased hole populations at the surface. Such a process could have hindered HT (Eqs. (15)–(17)) and even $^{\bullet}OH$ production (Eqs. (3)–(4)). It could have consequently diminished oxalate photodecomposition rates in the thickest O_2-free water films considered in this study. We however note that previous work [75] showed that trace (sub-ML) amounts of water could, instead, enhance hole mobility, at least at the scale of minutes. This consequently implies that these effects of (i) hindered HT and $^{\bullet}OH$ production in sub-ML and (ii) hydration-promoted electron trapping in larger ML films were manifested in the large range of water loadings (0.1–4 ML) considered in our study.

We consequently propose that (i) water film thickness, (ii) oxygen deficiency and (iii) accumulation of electrons in the shallow traps collectively contributed to hole localization. It also possible that photogenerated holes near sub-surfaces were more able to transfer to oxalate or water for photocatalytic reactions than photogenerated holes in in the bulk. This would explain the fast regime in the first 10 min, during which time only photogenerated holes on the surfaces were consumed, while other holes in the deeper regions were less dynamics and more localized at lattice/bulk O sites.

We also note that based on previous work, [73] proton rich water films could have also stabilized shallow trapped electrons (Eq. (12)), and thereby hampered electron-hole recombination and HT to oxalate. Once the trapping sites became saturated from the high electron density, which arose from hole consumption by oxalate, bulk holes slowly began to recombine, while still decomposing oxalate. This can be seen from the ~ 1^{st} up to the 20^{th} h of the reaction (Figs. Inset of 5c and S9). The drop in half-lives (Fig. 6e) and increase in yields (Fig. 6g) in the thicker water films revealed, in contrast, that (i) bulk holes successfully migrated to the surface to react with oxalate, or (ii) fresh holes were generated near the surface. The latter can occur if electron-hole recombination (Eq. (14)) happened, and a new cycle of electron-hole pair generation (Eq. (2)) under photoirradiation occurred.

Finally, we must emphasize that photoreactions in water-free TiO_2 had shorter half-lives (~ 2 h) and higher yields (~ 80 %) (Fig. 6g) than in the presence of water films. From the small and unstable STIRAs

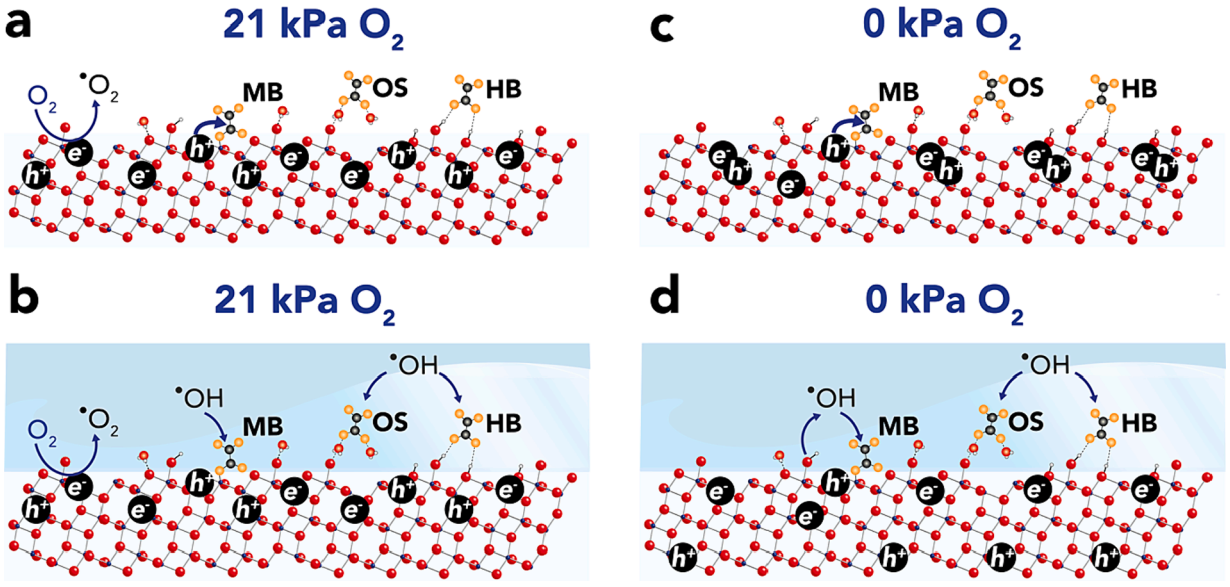

Fig. 7. Schematic representation of humidity- and oxygen-dependent photocatalytic decomposition of oxalate on TiO_2. (a) Nearly (0.0095 kPa H_2O) dry O_2-bearing conditions promote electron-scavenging ROS which enhances hole lifetimes. (b) Hydrated O_2-bearing conditions promote ROS and OH radical formation, as well as charge mobility. Oxalate oxidation proceeds via HT, LMCT and radical-driven reactions, which enhance reaction rates compared to the dry condition in (a). (c) Nearly (0.0095 kPa H_2O) dry O_2-free conditions promote oxalate oxidation by HT, and possibly LMCT because of the cycle of generation-recombination of electron-hole pairs. (d) Hydrated O_2-free conditions limit both charge mobility and ROS formation, thus decreasing oxalate oxidation rates. These conditions also generated STIRAs (Fig. 5 a-c).

(Fig. 6c & S8) we suggest that charge mobility was not greatly affected. We explain this by adapting a suggestion by Litke et al. [75], in which surface OH groups [76], formed by the dissociative binding of water in sub-ML films, trapped holes at faster rates than chemisorbed (undissociated) water. Because of these OH groups, holes can either recombine with electrons, producing unstable STIRAs, or participate in photoreactions with oxalate via bound $^{\bullet}$OH radicals (Eqs. (3)–(4)) and HT (Eqs. (15)–(18)). The photodecomposition rate did not slow down because fresh electron-hole pairs were continuously produced during irradiation after recombination. These holes were then able to preferentially oxidize the smaller surface loadings of oxalate (1.4 OX/nm^2) over the more abundant OH sites (~ 5 OH/nm^2) [64] – the sources of bound $^{\bullet}$OH radicals (Eq. (3b)). Still, we cannot discard LMCT as an additional pathway for decomposition.

3.3.3. *Photodecomposition affected by oxalate complexation modes*

Finally, we discuss how the oxalate binding modes controlled photodecomposition rate. In general, the rate loss of MB1 (1724 cm^{-1}) was more rapid than the MB2 (1690 cm^{-1}) and OS (1675 cm^{-1}) at all humidity ranges (Fig. 6f-g & S10), and this difference became important in O_2-free atmosphere. The photodecomposition trends of MB1 and MB2 were similar in both O_2-bearing and O_2-free atmospheres. OS complexes, on the other hand, shared similar photoreaction trends in the absence of O_2, yet their decomposition rates were unaffected by variations of humidity in the presence of O_2. While similar observations were previously made, [77] we can here explain these in terms of the different photochemical responses of MB and OS species.

These differences illustrate the case that oxalate decomposition did not solely proceed through a solvent-mediated $^{\bullet}$OH radical because this process would have unselectively oxidized all forms of oxalate. They show that HT and LMCT mechanisms in the absence of O_2 targeted the MB1 species, while decomposition rates of MB2 and OS were slower because $^{\bullet}$OH radical production was hampered by charge localization in thick water films. In this case, the hydration shell of the OS complex contributed to charge migration, explaining its reversal in reaction rates with humidity. Additionally, MB1 in both reaction atmospheres could undergo structural changes to MB2 before being finally decomposed, as previously suggested, [54] resulting in the slower disappearance of MB2. This mechanism could not be supported by our IR spectra because it likely happened at a faster rate than the spectral acquisition time (89 s).

As a result, we propose that MB2 and OS species were more resilient to decomposition via LMCT than MB1 species. The greater stability of MB2 and OS, again, can be justified by their first appearance upon adsorption experiment (Fig. 2c), even at low oxalate loadings. It was possible that MB2 adapted bridging (bidentate binuclear) or chelating (bidentate mononuclear) structures (Fig. 2b) for this high stability. MB1 could, on the other hand, have a monodentate structure, which is easier to decompose, and is a precursor species to MB2.[54]

4. Conclusions

Using vibrational spectroscopy, we resolved the water film-mediated photodecomposition of oxalate bound to TiO_2 nanoparticles. We find that thicker water films accelerated photocatalytic reaction rates for complete oxalate decomposition under atmospheric oxygen (21 kPa O_2) but decelerated the reactions in the absence of O_2. A schematic representation summarizing these effects is presented in Fig. 7. This contrasting effect can be attributed to the interplay of five key processes: (i) direct charge transfer between oxalate and TiO_2, involving hole transfer (HT) and ligand-to-metal charge transfer (LMCT), (ii) ROS production, (iii) solvent-mediated hydroxyl ($^{\bullet}$OH) radical oxidation, (iv) charge localization, and (v) charge recombination.

In the presence of oxygen (Fig. 7 a,b), HT/LMCT and ROS played a dominant role in driving the photodecomposition of oxalate on dehydrated TiO_2. The hydration environment of the films promoted water-mediated $^{\bullet}$OH radical production, which enhanced the reaction rates. Conversely, in the absence of oxygen (Fig. 7 c,d), water films induced charge localization on TiO_2 that stabilized shallow trap electrons. This, in turn, restricted hole oxidation for $^{\bullet}$OH production. In addition, the absence of O_2 as an electron scavenger suppressed the formation of $O_2^{\bullet-}$/$HO_2^{\bullet}$ radicals. Consequently, the photodecomposition of oxalate primarily proceeded through HT and LMCT, competed by electron-hole recombination that ultimately decreased reaction rate.

It is thus this interplay between surface loading, coordination environment (MB1 *vs.* MB2 *vs.* OS), water film thickness and oxygen availability that control the photostability of oxalate on TiO_2. By shedding new light on the water film-driven photodecomposition of oxalate by TiO_2, this work can help address the fate of organics in important natural (*e.g.* vadose zones of soils, atmospheric aerosol, *etc.*) and technological (*e.g.* wastewater treatment, air purification) settings.

CRediT authorship contribution statement

N. Tan Luong: Writing – review & editing, Writing – original draft, Visualization, Methodology, Investigation, Formal analysis, Data curation, Conceptualization. **Khalil Hanna:** Writing – review & editing. **Jean-François Boily:** Writing – review & editing, Supervision, Resources, Project administration, Methodology, Funding acquisition, Conceptualization.

Declaration of competing interest

The authors declare that they have no known competing financial interests or personal relationships that could have appeared to influence the work reported in this paper.

Data availability

Data will be made available on request.

Acknowledgements

This work was supported by the Swedish Research Council (2016-03808, 2020-04853) and FORMAS (2022-01246) to J.-F.B., and IRP CNRS CHEMICY (2023-2027) to J.-F.B. and K.H., and Styrelsen för Stiftelsen J C Kempes Minnes Stipendiefond to N.T.L. We thank Prof. Knut Irgum (Department of Chemistry, Umeå University), Chau Huynh (Northvolt AB), and Dr. Ngoc Phuoc Dinh (Klaria AB) for great support and assistance in the ion chromatography measurements.

Appendix A. Supplementary data

Supplementary data to this article can be found online at https://doi.org/10.1016/j.jcat.2024.115425.

References

[1] G.E. Ewing, Ambient thin film water on insulator surfaces, Chem. Rev. 106 (2006) 1511–1526.
[2] M. Yeşilbaş, J.-F. Boily, Particle size controls on water adsorption and condensation regimes at mineral surfaces, Sci. Rep. 6 (2016) 32136.
[3] M. Tang, D.J. Cziczo, V.H. Grassian, Interactions of water with mineral dust aerosol: water adsorption, hygroscopicity, cloud condensation, and ice nucleation, Chem. Rev. 116 (2016) 4205–4259.
[4] N.T. Luong, E.S. Ilton, A. Shchukarev, J.-F. Boily, Water film-driven mn (oxy)(hydr)oxide nanocoating growth on rhodochrosite, Geochim. Cosmochim. Acta 329 (2022) 87–105.
[5] C.E. Nanayakkara, W.A. Larish, V.H. Grassian, Titanium dioxide nanoparticle surface reactivity with atmospheric gases, CO2, SO2, and NO2: roles of surface hydroxyl groups and adsorbed water in the formation and stability of adsorbed products, J. Phys. Chem. C 118 (2014) 23011–23021.
[6] G.R. Bourret, O. Diwald, Thin water films covering oxide nanomaterials: stability issues and influences on materials processing, J. Mat. Res. 34 (2019) 428–441.
[7] G. Rubasinghege, V.H. Grassian, Role(s) of adsorbed water in the surface chemistry of environmental interfaces, Chem. Commun. 49 (2013) 3071–3094.

[8] H. Chen, C.E. Nanayakkara, V.H. Grassian, Titanium dioxide photocatalysis in atmospheric chemistry, Chem. Rev. 112 (2012) 5919–5948.
[9] T.A. Doane, A survey of photogeochemistry, Geochem. Trans. 18 (2017) 1.
[10] P.B. Amama, K. Itoh, M. Murabayashi, Photocatalytic oxidation of trichloroethylene in humidified atmosphere, J. Mol. Catal. a: Chem. 176 (2001) 165–172.
[11] W. Wang, L.-W. Chiang, Y. Ku, Decomposition of benzene in air streams by UV/TiO2 process, J. Hazard. Mater. 101 (2003) 133–146.
[12] K. Demeestere, J. Dewulf, B. De Witte, A. Beeldens, H. Van Langenhove, Heterogeneous photocatalytic removal of toluene from air on building materials enriched with TiO2, Build. Environm. 43 (2008) 406–414.
[13] A. Alonso-Tellez, D. Robert, N. Keller, V. Keller, A parametric study of the UV-A photocatalytic oxidation of H2S over TiO2, Appl. Catal., B 115–116 (2012) 209–218.
[14] M. Schreck, M. Niederberger, Photocatalytic gas phase reactions, Chem. Mater. 31 (2019) 597–618.
[15] K. Sivula, F. Le Formal, M. Grätzel, Solar water splitting: Progress using hematite (α-Fe2O3) photoelectrodes, ChemSusChem 4 (2011) 432–449.
[16] Y. Ma, X. Wang, Y. Jia, X. Chen, H. Han, C. Li, Titanium dioxide-based nanomaterials for photocatalytic fuel generations, Chem. Rev. 114 (2014) 9987–10043.
[17] K. Brinkert, C. Zhuang, M. Escriba-Gelonch, V. Hessel, The potential of catalysis for closing the loop in human space exploration, Catal. Today 423 (2023) 114242.
[18] K. Hans Wedepohl, The composition of the continental crust, Geochim. Cosmochim. Acta 59 (1995) 1217–1232.
[19] M.A. Henderson, A surface science perspective on TiO2 photocatalysis, Surf. Sci. Rep. 66 (2011) 185–297.
[20] U. Diebold, The surface science of titanium dioxide, Surf. Sci. Rep. 48 (2003) 53–229.
[21] T.L. Thompson, J.T. Yates, Surface science studies of the photoactivation of TiO2New photochemical processes, Chem. Rev. 106 (2006) 4428–4453.
[22] Y. Nosaka, Water photo-oxidation over TiO2-history and reaction mechanism, Catalysts (2022).
[23] K. Bourikas, C. Kordulis, A. Lycourghiotis, Titanium dioxide (anatase and rutile): surface chemistry, liquid-solid Interface chemistry, and scientific synthesis of supported catalysts, Chem. Rev. 114 (2014) 9754–9823.
[24] A. Fujishima, X. Zhang, D.A. Tryk, TiO2 photocatalysis and related surface phenomena, Surf. Sci. Rep. 63 (2008) 515–582.
[25] C.E. Nanayakkara, J.K. Dillon, V.H. Grassian, Surface adsorption and photochemistry of gas-phase formic acid on TiO2 nanoparticles: the role of adsorbed water in surface coordination, adsorption kinetics, and rate of photoproduct formation, J. Phys. Chem. C 118 (2014) 25487–25495.
[26] H. Park, Y. Park, W. Kim, W. Choi, Surface modification of TiO2 photocatalyst for environmental applications, J. Photochem. Photobiol., C 15 (2013) 1–20.
[27] R. Daghrir, P. Drogui, D. Robert, Modified TiO2 for environmental photocatalytic applications: a review, Ind. Eng. Chem. Res. 52 (2013) 3581–3599.
[28] S.G. Kumar, L.G. Devi, Review on modified TiO2 photocatalysis under UV/VISIBLE light: selected results and related mechanisms on interfacial charge carrier transfer dynamics, J. Phys. Chem. A 115 (2011) 13211–13241.
[29] L. Mino, A. Zecchina, G. Martra, A.M. Rossi, G. Spoto, A surface science approach to TiO2 P25 photocatalysis: an in situ FTIR study of phenol photodegradation at controlled water coverages from sub-monolayer to multilayer, Appl. Catal., B 196 (2016) 135–141.
[30] G. Martra, S. Coluccia, L. Marchese, V. Augugliaro, V. Loddo, L. Palmisano, M. Schiavello, The role of H2O in the photocatalytic oxidation of toluene in vapour phase on anatase TiO2 catalyst: a FTIR study, Catal. Today 53 (1999) 695–702.
[31] G. Marcì, M. Addamo, V. Augugliaro, S. Coluccia, E. García-López, V. Loddo, G. Martra, L. Palmisano, M. Schiavello, Photocatalytic oxidation of toluene on irradiated TiO2: comparison of degradation performance in humidified air, in water and in water containing a zwitterionic surfactant, J. Photochem. Photobiol., A 160 (2003) 105–114.
[32] M. Takeuchi, J. Deguchi, S. Sakai, M. Anpo, Effect of H2O vapor addition on the photocatalytic oxidation of ethanol, acetaldehyde and acetic acid in the gas phase on TiO2 semiconductor powders, Appl. Catal., B 96 (2010) 218–223.
[33] H.O. Seo, E.J. Park, I.H. Kim, S.W. Han, B.J. Cha, T.G. Woo, Y.D. Kim, Influence of humidity on the photo-catalytic degradation of acetaldehyde over TiO2 surface under UV light irradiation, Catal. Today 295 (2017) 102–109.
[34] Z. Yu, S.S.C. Chuang, In situ IR study of adsorbed species and photogenerated electrons during photocatalytic oxidation of ethanol on TiO2, J. Catal. 246 (2007) 118–126.
[35] C. Richard, Regioselectivity of oxidation by positive holes (h+) in photocatalytic aqueous transformations, J. Photochem. Photobiol., A 72 (1993) 179–182.
[36] T.N. Obee, S.O. Hay, Effects of moisture and temperature on the photooxidation of ethylene on titania, Environ. Sci. Technol. 31 (1997) 2034–2038.
[37] B. Liu, X. Zhao, J. Yu, I.P. Parkin, A. Fujishima, K. Nakata, Intrinsic intermediate gap states of TiO2 materials and their roles in charge carrier kinetics, J. Photochem. Photobiol., C, 39 (2019) 1-57.
[38] S. Selcuk, A. Selloni, Facet-dependent trapping and dynamics of excess electrons at anatase TiO2 surfaces and aqueous interfaces, Nat. Mater. 15 (2016) 1107–1112.
[39] J. Cheng, J. VandeVondele, M. Sprik, Identifying trapped electronic holes at the aqueous TiO2 Interface, J. Phys. Chem. C 118 (2014) 5437–5444.
[40] J. Baltrusaitis, J. Schuttlefield, J.H. Jensen, V.H. Grassian, FTIR spectroscopy combined with quantum chemical calculations to investigate adsorbed nitrate on aluminium oxide surfaces in the presence and absence of co-adsorbed water, Phys. Chem. Chem. Phys. 9 (2007) 4970–4980.
[41] T.M. Miller, V.H. Grassian, Heterogeneous chemistry of NO2 on mineral oxide particles: spectroscopic evidence for oxide-coordinated and water-solvated surface nitrate, Geophys. Res. Lett. 25 (1998) 3835–3838.
[42] A. Sorooshian, Z. Wang, M.M. Coggon, H.H. Jonsson, B. Ervens, Observations of sharp oxalate reductions in stratocumulus clouds at variable altitudes: organic acid and metal measurements during the2011 E-PEACE campaign, Environ. Sci. Technol. 47 (2013) (2011) 7747–7756.
[43] G. Sposito, The chemistry of soils, 3rd ed., Oxford University Press, 2016.
[44] J. Bangun, A.A. Adesina, The photodegradation kinetics of aqueous sodium oxalate solution using TiO2 catalyst, Appl. Catal. General 175 (1998) 221–235.
[45] A. Verma, R. Kore, D.R. Corbin, M.B. Shiflett, Metal recovery using oxalate chemistry: a technical review, Ind. Eng. Chem. Res. 58 (2019) 15381–15393.
[46] J.-M. Herrmann, M.-N. Mozzanega, P. Pichat, Oxidation of oxalic acid in aqueous suspensions of semiconductors illuminated with UV or visible light, J. Photochem. 22 (1983) 333–343.
[47] T. Preočanin, N. Kallay, Point of zero charge and surface charge density of TiO2 in aqueous electrolyte solution as obtained by potentiometric mass titration, Croatica Chemica Acta 79 (2006) 95–106.
[48] S.J. Hug, B. Sulzberger, In situ fourier transform infrared spectroscopic evidence for the formation of several different surface complexes of oxalate on TiO2 in the aqueous phase, Langmuir 10 (1994) 3587–3597.
[49] S.J. Hug, D. Bahnemann, Infrared spectra of oxalate, malonate and succinate adsorbed on the aqueous surface of rutile, anatase and lepidocrocite measured with in situ ATR-FTIR, J. Electron Spectrosc. Relat. Phenom. 150 (2006) 208–219.
[50] C.B. Mendive, T. Bredow, A. Feldhoff, M.A. Blesa, D. Bahnemann, Adsorption of oxalate on anatase (100) and rutile (110) surfaces in aqueous systems: experimental results vs. theoretical predictions, Phys. Chem. Chem. Phys. 11 (2009) 1794–1808.
[51] M.M. Kosanić, Photocatalytic degradation of oxalic acid over TiO2 power, J. Photochem. Photobiol., A 119 (1998) 119–122.
[52] C.B. Mendive, D.W. Bahnemann, M.A. Blesa, Microscopic characterization of the photocatalytic oxidation of oxalic acid adsorbed onto TiO2 by FTIR-ATR, Catal. Today 101 (2005) 237–244.
[53] C.B. Mendive, T. Bredow, M.A. Blesa, D.W. Bahnemann, ATR-FTIR measurements and quantum chemical calculations concerning the adsorption and photoreaction of oxalic acid on TiO2, Phys. Chem. Chem. Phys. 8 (2006) 3232–3247.
[54] C.B. Mendive, T. Bredow, J. Schneider, M. Blesa, D. Bahnemann, Oxalic acid at the TiO2/water interface under UV(A) illumination: surface reaction mechanisms, J. Catal. 322 (2015) 60–72.
[55] J. Park, G.-H. Moon, K.-O. Shin, J. Kim, Oxalate-TiO2 complex-mediated oxidation of pharmaceutical pollutants through ligand-to-metal charge transfer under visible light, Chem. Eng. J. 343 (2018) 689–698.
[56] X. Jiang, M. Manawan, T. Feng, R. Qian, T. Zhao, G. Zhou, F. Kong, Q. Wang, S. Dai, J.H. Pan, Anatase and rutile in evonik aeroxide P25: heterojunctioned or individual nanoparticles? Catal. Today 300 (2018) 12–17.
[57] L. Mino, G. Spoto, S. Bordiga, A. Zecchina, Particles morphology and surface properties as investigated by HRTEM, FTIR, and periodic DFT calculations: from pyrogenic TiO2 (P25) to nanoanatase, J. Phys. Chem. C 116 (2012) 17008–17018.
[58] G. Martra, Lewis acid and base sites at the surface of microcrystalline TiO2 anatase: relationships between surface morphology and chemical behaviour, Appl. Catal. General 200 (2000) 275–285.
[59] S. Brunauer, P.H. Emmett, E. Teller, Adsorption of gases in multimolecular layers, J. Am. Chem. Soc. 60 (1938) 309–319.
[60] X. Song, J.-F. Boily, Water vapor interactions with FeOOH particle surfaces, Chem. Phys. Lett. 560 (2013) 1–9.
[61] J.-F. Boily, M. Yeşilbaş, M.M. Musleh Uddin, L. Baiqing, Y. Trushkina, G. Salazar-Alvarez, Thin water films at multifaceted hematite particle surfaces, Langmuir 31 (2015) 13127–13137.
[62] J.F. Boily, L. Fu, A. Tuladhar, Z. Lu, B.A. Legg, Z.M.M. Wang, H.F. Wang, Hydrogen bonding and molecular orientations across thin water films on sapphire, J. Colloid Interface Sci. 555 (2019) 810–817.
[63] J. Jaumot, R. Gargallo, A. de Juan, R. Tauler, A graphical user-friendly interface for MCR-ALS: a new tool for multivariate curve resolution in MATLAB, Chem. Intel. Lab. Sys. 76 (2005) 101–110.
[64] R. Mueller, H.K. Kammler, K. Wegner, S.E. Pratsinis, OH surface density of SiO2 and TiO2 by thermogravimetric analysis, Langmuir 19 (2003) 160–165.
[65] I. Ivanova, C.B. Mendive, D. Bahnemann, The role of nanoparticulate agglomerates in TiO2 photocatalysis: degradation of oxalic acid, J. Nanoparticle Res. 18 (2016) 187.
[66] P. Persson, K. Axe, Adsorption of oxalate and malonate at the water-goethite interface: molecular surface speciation from IR spectroscopy, Geochim. Cosmochim. Acta 69 (2005) 541–552.
[67] D. Biriukov, O. Kroutil, M. Kabeláč, M.K. Ridley, M.L. Machesky, M. Předota, Oxalic acid adsorption on rutile: molecular dynamics and ab initio calculations, Langmuir 35 (2019) 7617–7630.
[68] J. Rosenqvist, K. Axe, S. Sjöberg, P. Persson, Adsorption of dicarboxylates on nano-sized gibbsite particles: effects of ligand structure on bonding mechanisms, colloids surf, A 220 (2003) 91–104.
[69] A.G. Young, A.J. McQuillan, Adsorption/Desorption kinetics from ATR-IR spectroscopy. aqueous oxalic acid on anatase TiO2, Langmuir 25 (2009) 3538–3548.
[70] W.J. Smit, F. Tang, M.A. Sánchez, E.H.G. Backus, L. Xu, T. Hasegawa, M. Bonn, H. J. Bakker, Y. Nagata, Excess hydrogen bond at the ice-vapor Interface around 200 K, Physical Review Letters 119 (2017) 133003.

[71] P. Jones, J.A. Hockey, Infra-red studies of rutile surfaces. part 2. —Hydroxylation, hydration and structure of rutile surfaces, Trans. Faraday Soc. 67 (1971) 2679–2685.
[72] M.R. Hoffmann, S.T. Martin, W. Choi, D.W. Bahnemann, Environmental applications of semiconductor photocatalysis, Chem. Rev. 95 (1995) 69–96.
[73] D.M. Savory, A.J. McQuillan, Influence of formate adsorption and protons on shallow trap infrared absorption (STIRA) of anatase TiO2 during photocatalysis, J. Phys. Chem. C 117 (2013) 23645–23656.
[74] L.A. Lyon, J.T. Hupp, Energetics of the nanocrystalline titanium dioxide/aqueous solution Interface: approximate conduction band edge variations between H0 = −10 and H- = +26, J. Phys. Chem. B 103 (1999) 4623–4628.
[75] A. Litke, Y. Su, I. Tranca, T. Weber, E.J.M. Hensen, J.P. Hofmann, Role of adsorbed water on charge carrier dynamics in photoexcited TiO2, J. Phys. Chem. C 121 (2017) 7514–7524.
[76] F. Fasulo, G. Piccini, A.B. Muñoz-García, M. Pavone, M. Parrinello, Dynamics of water dissociative adsorption on TiO2 anatase (101) at monolayer coverage and below, J. Phys. Chem. C 126 (2022) 15752–15758.
[77] P.Z. Araujo, C.B. Mendive, L.A.G. Rodenas, P.J. Morando, A.E. Regazzoni, M. A. Blesa, D. Bahnemann, FT-IR–ATR as a tool to probe photocatalytic interfaces, Colloids Surf. A 265 (2005) 73–80.